

## Direct retrieval of sulfur dioxide amount and altitude from spaceborne hyperspectral UV measurements: Theory and application

Kai Yang,<sup>1,2</sup> Xiong Liu,<sup>1,2</sup> Pawan K. Bhartia,<sup>2</sup> Nickolay A. Krotkov,<sup>1,2</sup> Simon A. Carn,<sup>3</sup> Eric J. Hughes,<sup>4</sup> Arlin J. Krueger,<sup>4</sup> Robert J. D. Spurr,<sup>5</sup> and Samuel G. Trahan<sup>6</sup>

Received 31 January 2010; revised 3 June 2010; accepted 9 June 2010; published 21 September 2010.

[1] We describe the physical processes by which a vertically localized absorber perturbs the top-of-atmosphere solar backscattered ultraviolet (UV) radiance. The distinct spectral responses to perturbations of an absorber in its column amount and layer altitude provide the basis for a practical satellite retrieval technique, the Extended Iterative Spectral Fitting (EISF) algorithm, for the simultaneous retrieval of these quantities of a SO<sub>2</sub> plume. In addition, the EISF retrieval provides an improved UV aerosol index for quantifying the spectral contrast of apparent scene reflectance at the bottom of atmosphere bounded by the surface and/or cloud; hence it can be used for detection of the presence or absence of UV absorbing aerosols. We study the performance and characterize the uncertainties of the EISF algorithm using synthetic backscattered UV radiances, retrievals from which can be compared with those used in the simulation. Our findings indicate that the presence of aerosols (both absorbing and nonabsorbing) does not cause large errors in EISF retrievals under most observing conditions when they are located below the SO<sub>2</sub> plume. The EISF retrievals assuming a homogeneous field of view can provide accurate column amounts for inhomogeneous scenes, but they always underestimate the plume altitudes. The EISF algorithm reduces systematic errors present in existing linear retrieval algorithms that use prescribed SO<sub>2</sub> plume heights. Applying the EISF algorithm to Ozone Monitoring Instrument satellite observations of the recent Kasatochi volcanic eruption, we demonstrate the successful retrieval of effective plume altitude of volcanic SO<sub>2</sub>, and we also show the improvement in accuracy in the corresponding SO<sub>2</sub> columns.

**Citation:** Yang, K., X. Liu, P. K. Bhartia, N. A. Krotkov, S. A. Carn, E. J. Hughes, A. J. Krueger, R. J. D. Spurr, and S. G. Trahan (2010), Direct retrieval of sulfur dioxide amount and altitude from spaceborne hyperspectral UV measurements: Theory and application, *J. Geophys. Res.*, 115, D00L09, doi:10.1029/2010JD013982.

### 1. Introduction

[2] Volcanic SO<sub>2</sub>, upon oxidation in the atmosphere, is converted into sulfuric aerosols; these may have long residence times (up to a few years), depending mostly on their altitudes in the atmosphere. These aerosols affect radiative forcing directly by reflecting the incoming solar radiation and indirectly by changing the albedo and lifetime of clouds [Bréon *et al.*, 2002; Gassó, 2008, and references therein]. Large eruptions throughout history are known to have influenced the global or hemispheric climate [Robock,

2000]. The strongest eruption in the twentieth century (Pinatubo, June 1991), released about 20 million tons (Mt) of SO<sub>2</sub> [Bluth *et al.*, 1992] directly into the stratosphere and caused an average global cooling of 0.3°C that lasted for about 2 years [Robock, 2000]. Although eruptions of the magnitude of Pinatubo occur rarely (maybe once in a century), volcanic degassing is continuous and smaller eruptions occur sporadically (a few times in a year) in various regions. Usually, a single eruption does not have significant impact beyond the immediate area surrounding the volcano, but cumulative contributions from volcanic emissions (large and small) over the globe play a major role in regulating the burden of sulfuric aerosols in the troposphere and stratosphere [Vernier *et al.*, 2009]. In order to understand their impacts on atmospheric chemistry and climate, it is important to measure both the abundance and altitude of these volcanic SO<sub>2</sub> emissions. These SO<sub>2</sub> data also provide critical information for aviation hazard mitigation, when they are distributed in near real time to the Volcanic Ash Advisory Centers (VAACs) [Carn *et al.*, 2008]. The basis for this application is that the presence of SO<sub>2</sub> is a robust indication of explosive magmatic eruptions, which often inject ash

<sup>1</sup>Goddard Earth Sciences and Technology Center, University of Maryland Baltimore County, Baltimore, Maryland, USA.

<sup>2</sup>Laboratory for Atmospheres, NASA Goddard Space Flight Center, Greenbelt, Maryland, USA.

<sup>3</sup>Michigan Technological University, Houghton, Michigan, USA.

<sup>4</sup>Joint Center for Earth Systems Technology, University of Maryland Baltimore County, Baltimore, Maryland, USA.

<sup>5</sup>RT Solutions, Inc., Cambridge, Massachusetts, USA.

<sup>6</sup>Department of Physics, University of Maryland Baltimore County, Baltimore, Maryland, USA.

(comprising pulverized rock and glass) that are initially collocated with the emitted SO<sub>2</sub> in the atmosphere.

[3] Satellite remote sensing can provide valuable globally based information on volcanic activity over the globe. A unique long-term record of volcanic SO<sub>2</sub> emissions [Carn *et al.*, 2003] has been derived from observations taken by the polar-orbiting Total Ozone Monitoring Spectrometers (TOMS) [Krueger *et al.*, 1995], which were in operation near continuously from 1978 to 2005. This record contains total SO<sub>2</sub> burdens from explosive eruptions only, due to the limited sensitivity of TOMS measurements to low SO<sub>2</sub> column densities. New-generation satellite instruments, such as the polar-orbiting hyperspectral ultraviolet (UV) and infrared (IR) sensors, and advances in retrieval techniques have expanded our ability to measure volcanic emissions [Clarisse *et al.*, 2008; Eckhardt *et al.*, 2008; Yang *et al.*, 2009a, 2009b]. In this paper, we use a new direct spectral fitting algorithm to perform simultaneous retrievals of SO<sub>2</sub> burdens and plume heights from observations of the 2008 Kasatochi eruption (Aleutian Islands, Alaska) made by the Dutch-Finnish Ozone Monitoring Instrument (OMI) [Levelt *et al.*, 2006a] on board NASA's Aura satellite.

[4] A number of algorithms have been developed to extract vertical SO<sub>2</sub> columns from satellite backscattered ultraviolet (BUV) measurements. To date, these algorithms have used the assumption that perturbations to the logarithm of the top-of-atmosphere (TOA) radiance are proportional to the SO<sub>2</sub> concentration along the effective photon path length. These algorithms include the standard Differential Optical Absorption Spectroscopy (DOAS) [Platt, 1994] method applied to SO<sub>2</sub> retrievals [Eisinger and Burrows, 1998; Khokhar *et al.*, 2005], the weighting function DOAS (WFDOAS) for SO<sub>2</sub> [Lee *et al.*, 2008], the Band Residual Difference (BRD) method [Krotkov *et al.*, 2006] developed for the OMI operational planetary-boundary-layer (PBL) product, and the Linear Fit (LF) algorithm [Yang *et al.*, 2007] used for OMI volcanic SO<sub>2</sub> products. Note that the WFDOAS, when applied to ozone retrieval [Coldewey-Egbers *et al.*, 2005], uses an iterative retrieval approach, which does not make the linear response assumption. However, the WFDOAS for SO<sub>2</sub> retrieval has used a hybrid approach: iterative retrieval for ozone and standard DOAS for SO<sub>2</sub> [Lee *et al.*, 2008]. Thus far, the WFDOAS applied to SO<sub>2</sub> is still a linear method.

[5] The assumption of linear response is valid when the SO<sub>2</sub> absorption optical thickness is small. However, this assumption is no longer valid when absorber amounts are large, and in these cases, linear algorithms can result in significant SO<sub>2</sub> underestimation as illustrated by Yang *et al.* [2009a]. These linear techniques also rely on a priori SO<sub>2</sub> vertical distributions (usually characterized by plume altitudes) in computing air mass factors (AMFs) for DOAS or the BRD or weighting functions for LF and WFDOAS. This can result in retrieval errors that increase with growing differences between the prescribed and the actual SO<sub>2</sub> plume altitudes.

[6] To overcome the disadvantages associated with existing linear algorithms, we have recently developed a new technique [Yang *et al.*, 2009b] by extending the iterative spectral fitting (ISF) algorithm [Yang *et al.*, 2009a] to determine the effective SO<sub>2</sub> plume altitude simultaneously along with the vertical columns of ozone and SO<sub>2</sub>. In this paper, we provide a detailed description of the physical

mechanisms behind the extended ISF (EISF) technique. We use closed-loop EISF testing to study the impacts of two important factors (spatial inhomogeneity and the presence of aerosols), on the retrieved SO<sub>2</sub> column and altitude. We then apply the EISF algorithm to OMI observations of the August 2008 Kasatochi eruption, providing a direct estimate of SO<sub>2</sub> vertical columns of the plumes and their corresponding heights. Finally, comparisons of retrieved plume heights with collocated backscatter vertical distribution measured by the Cloud-Aerosol Lidar with Orthogonal Polarization (CALIOP) on board the Cloud-Aerosol Lidar and Infrared Pathfinder Satellite Observation (CALIPSO) satellite [Winker *et al.*, 2003], and with plume heights estimated from trajectory modeling are presented.

## 2. Measurement of Trace Gases in the UV

[7] For UV backscatter, it is convenient to use the radiance contribution function [Bhartia *et al.*, 1996] to describe the contribution to the measured radiance from photons last backscattered toward the satellite sensor at different atmospheric levels. The area to the left of one radiance contribution function (Figure 1) represents the sum of photons from all atmospheric levels, and is thus a proxy for the magnitude of the TOA radiance. Note that in the case of normalized radiance contribution function (Figure 1), this area is equal to 1.

[8] In Figure 1, radiance contribution functions peak at lower atmospheric levels with increasing wavelengths; this is the key principle behind the BUV (backscatter UV) measurement technique for absorbing trace gases. Physically, more solar photons penetrated deeper into atmosphere as a result of weaker ozone absorption and Rayleigh scattering at longer wavelengths. In the wavelength range 255–335 nm, the altitude of maximum contribution moves progressively to lower levels of the atmosphere and the contribution peaks in the lower troposphere for wavelengths longer than 320 nm. In other words, a measured UV spectrum in this wavelength range is equivalent to a vertical scan down to the bottom of the atmosphere, therefore carrying information about the constituent absorbers, including their column amounts and vertical distributions. At wavelengths shorter than 300 nm, strong ozone absorption is the dominant factor limiting the penetration depth of the photons to the stratosphere, while at wavelengths longer than 304 nm, weaker ozone absorption and Rayleigh scattering allows photons to reach deeper into the troposphere. At wavelengths longer than 310 nm, photons backscattered from the lower troposphere comprise the dominant contribution to the TOA radiance, and most of measured TOA photons at these wavelengths have traversed through the entire atmosphere, from the top to the lower troposphere before being backscattered.

[9] We consider an idealized case, in which the absorber is vertically localized in an infinitesimal layer and multiple scattering is neglected. The TOA radiance  $I_{TOA}$  for a single wavelength (not labeled explicitly) can then be expressed as

$$I_{TOA}(N, z) = I_a(z) + e^{-m\tau_a} I_b(z), \quad (1)$$

where  $I_a(z) = \int_z^\infty C(z') dz'$  and  $I_b(z) = \int_0^z C(z') dz'$  are the contributions to TOA radiance from the regions above and

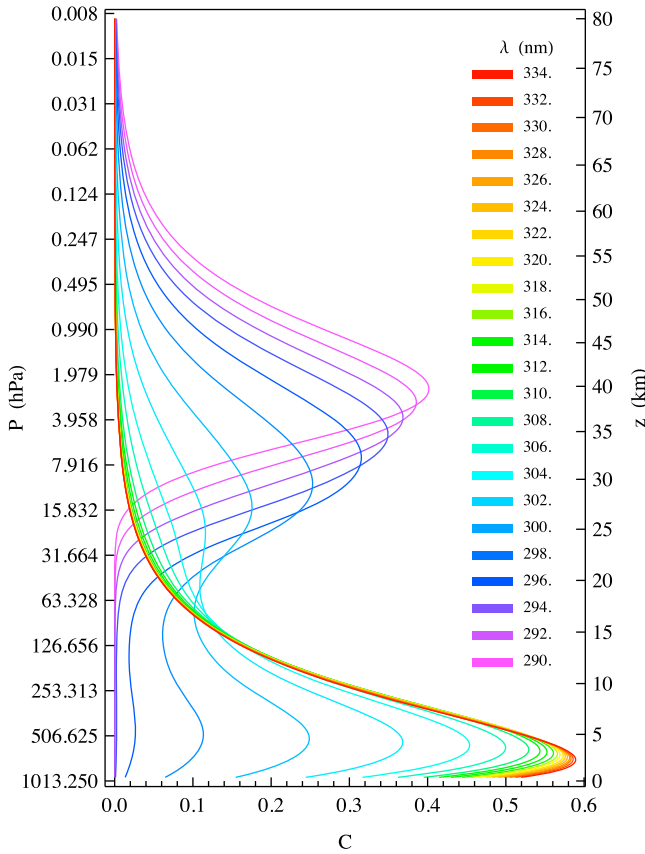


**Figure 1.** Radiance contribution functions ( $C$ ) for a set of UV wavelengths for a cloud and aerosol-free atmosphere with ozone absorption (TOMS V8 [Bhartia and Wellemeyer, 2002] standard midlatitude profile with total amount 275 Dobson units, where 1 DU =  $2.69 \times 10^{16}$  molecules/cm<sup>2</sup>). Calculations were done for nadir viewing geometry, 45° solar zenith angle, and a Lambertian surface reflectivity set to 0.05 at the bottom of the atmosphere. Results are normalized by the TOA radiance, i.e., the area formed by a curve and the  $\ln P$  axis is equal to one.

below the absorbing layer, respectively;  $C(z)$  is the radiance contribution function defined in the beginning of this section;  $\tau_a = \sigma_a N$ , is the absorbing optical thickness of the layer with absorber column amount  $N$  and absorption cross section  $\sigma_a$ ;  $z$  is the layer altitude and  $z'$  is the vertical coordinate of the atmosphere;  $m = \sec\theta_0 + \sec\theta$ , is the geometrical air mass factor (AMF) for solar zenith angle ( $\theta_0$ ) and viewing zenith angle ( $\theta$ ). In writing equation (1), we have made the weak absorber assumption, which requires that the introduction of additional absorber layer at  $z$  does not affect the radiance contribution function  $C(z)$ , and therefore  $I_a(z)$  and  $I_b(z)$ .

## 2.1. Absorber Column

[10] The spectral absorption signature of a trace gas identifies its presence. The DOAS method derives the column amount  $N$  by comparing the differential structure in  $\ln I_{TOA}$  with the differential absorption cross section  $\sigma_a$ ,

$$\frac{\partial \ln I_{TOA}}{\partial \sigma_a} = -m' N, \quad (2)$$

where

$$m' = m \frac{e^{-m\tau_a} I_b(z)}{I_{TOA}(N, z)} = m \left( 1 - \frac{I_a(z)}{I_{TOA}(N, z)} \right), \quad (3)$$

is the AMF. Equation (3) states that the geometrical air mass factor is scaled by the fraction of the radiance coming from below the absorbing layer, showing that  $m'$  in general depends on wavelength (not labeled explicitly), layer altitude  $z$ , and the absorber amount  $N$ . Under the weak absorption assumption, the AMF dependence on column amount is neglected (this is the linear response regime). AMF wavelength dependence may be minimized by the proper selection of fitting window size and location.

[11] The LF method is based on the weighting functions (WF) (also known as Jacobians) with respect to the vertical column amount  $N$  (evaluated at  $N = 0$ ),

$$\left. \frac{\partial \ln I_{TOA}}{\partial N} \right|_{N=0} = -\sigma_a m'. \quad (4)$$

These are used as the fitting reference spectra (in place of absorption cross sections) to model the observed spectral structures in the logarithm of  $I_{TOA}$ . This eliminates the inherent DOAS drawback of using a single wavelength AMF for the entire spectral fitting window.

[12] In cases of strong absorption, the linear response is no longer valid, in that the observed differential spectral structures in the measurements are no longer proportional to the amount of absorber. Linear methods then tend to underestimate the actual absorber columns, because the AMFs or WFs calculated in the linear regime would usually be larger than that for the strong absorption (nonlinear) cases. However column retrievals for these cases can be properly handled with an iterative approach, such as the ISF method [Yang *et al.*, 2009a] or the WFDOAS [Coldewey-Egbers *et al.*, 2005] and GODFIT techniques [Lerot *et al.*, 2010]. In the ISF approach, the linear LF retrieval is repeated at each iteration (linearization point), so that the WF is updated through

$$\left. \frac{\partial \ln I_{TOA}}{\partial N} \right|_{N=N_i} = -\sigma_a m'_i. \quad (5)$$

Here  $m'_i$  is similar to that defined in equation (3), but with  $I_a$  and  $I_{TOA}$  computed with the atmospheric conditions and the absorber column  $N_i$  at the  $i$ th iteration.

[13] In order to retrieve accurately the vertical column of an absorber, all these methods need a proper assignment of its vertical profile when calculating the AMFs or WFs. Information about the absorber vertical distribution (especially when the absorber is confined to a small altitude range) is contained in BUUV spectra as described earlier in this section, and in section 2.2 we examine how this vertical information can be separated from that of the absorber column, thereby extracting both from BUUV spectral measurements.

## 2.2. Absorber Altitude

[14] We want to show that the effect of layer altitude change on TOA radiance can be distinguished from that of column change. Different physical mechanisms are responsible for absorption perturbations: A change in layer

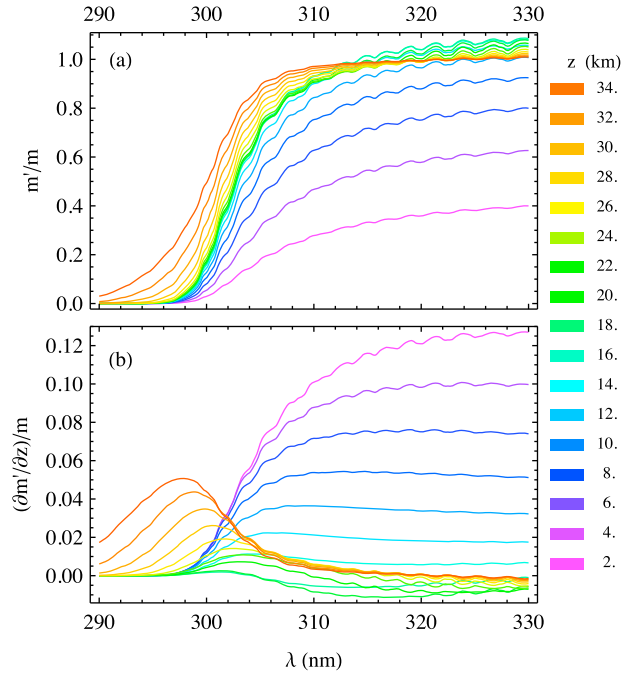


**Figure 2.** AMF ( $m'$ ), normalized by (a) the geometrical AMF ( $m$ ) and (b) its vertical gradient ( $\partial m'/\partial z/m$ ). Calculations for the same conditions as in Figure 1.

amount  $N$  has a direct effect on the layer absorption optical thickness, while a change in the layer altitude  $z$  directly effects the number of photons passing through the layer and, in the case of temperature-dependent absorption, may also induce a change in the layer absorption optical thickness due to the temperature variation with altitude. These physical mechanisms generate different responses in the TOA radiance, whose sensitivities are described by the respective WFs. The WF with respect to the layer altitude  $z$  (assuming  $\sigma_a$  is independent of  $z$ , i.e., it has no temperature dependence) is

$$\frac{\partial \ln I_{TOA}}{\partial z} = (e^{-m\tau_a} - 1) \frac{C(z)}{I_{TOA}} = -m\tau_a \frac{C(z)}{I_{TOA}} \quad (6)$$

$$= -\tau_a \frac{\partial m'}{\partial z} \left/ \left( 1 - \tau_a (m - m') \right) \right. \quad (7)$$

$$= -N\sigma_a \frac{\partial m'}{\partial z}. \quad (8)$$

Starting from equation (1), we have used these equations,  $\partial I_a(z)/\partial z = -C(z)$  and  $\partial I_b(z)/\partial z = C(z)$ , the weak absorption assumption, i.e.,  $e^{-m\tau_a} - 1 \approx -m\tau_a$ , and

$$\partial m'/\partial z \approx m \left( 1 - m\tau_a \frac{I_a(z)}{I_{TOA}} \right) \frac{C(z)}{I_{TOA}} = m \left( 1 - \tau_a (m - m') \right) \frac{C(z)}{I_{TOA}}, \quad (9)$$

in deriving equations (6) and (7). Keeping only the first-order term of  $\tau_a = N\sigma_a$ , we arrive at equation (8) from (7).

Comparing equations (4) and (8), one can see that the layer column WF (equation (4)) is proportional to the local AMF  $m'$ , while the altitude WF (equation (8)) is proportional to its vertical gradient at  $z$ , with the absorber cross section as a common factor in both expressions. These relationships between local AMF and layer column and altitude WFs are quite general and have been established by Yang *et al.* [2009b] without the single-scattering assumption used in equation (1), though the weak absorption assumption is still required.

[15] Equation (3) shows that the altitude-dependent AMF  $m'(z)$  is proportional to the total photon contribution to TOA radiance from below the absorber layer  $I_b(z)$ , which is the integral of radiance contribution function ( $C(z)$ ) from the ground up to the layer altitude  $z$ . Conversely, the AMF vertical gradient (equation (6)) is proportional to  $C(z)$  only. The radiance contribution function  $C(z)$  strongly depends on both (see Figure 1) wavelength and altitude, resulting in distinctive spectral dependences in the AMF and its vertical gradient. This is seen clearly in Figure 2, which illustrates sensitivity in part of the UV spectrum to the absorber amount and altitude. Results for AMFs and their gradients were calculated with the vector linearized discrete ordinate radiative transfer code (VLIDORT) [Spurr, 2008] that includes polarization, multiple scattering, and pseudo-spherical corrections. Note that the larger the AMF, the more sensitive the TOA radiance to absorber amount is, and the steeper the AMF gradient, the more sensitive to absorber altitude. It is also important to point out that the altitude WF (equation (8)) is proportional to the layer column  $N$ , indicating that noticeable TOA radiance response to altitude change can be observed only when there is a significant amount of absorber. Furthermore, when  $\tau_a$  increases, the height sensitivity is likely to increase as well according to equation (7), because in general (but not always)  $m > m'$  (see Figure 2a);  $m < m'$  happens only when the absorber is high in the atmosphere ( $>15$  km) for longer wavelengths ( $>315$  nm). These are the conditions under which the single scattering approximation is apparently not valid.

[16] The AMF and its vertical gradient describe the general atmospheric characteristics resulting from the differential vertical sampling by photons at different wavelengths. These are the common factors in the respective (column and altitude) WFs of any trace gas that absorbs radiation. Clearly the layer column and altitude WFs are correlated, since both of them (equations (4) and (8)) are proportional to the trace gas absorption cross section. This is seen in Figure 3 for SO<sub>2</sub>: Both WFs exhibit the same high-frequency structure. Because of this correlation, it may be difficult in a narrow spectral window to distinguish the effect of a column perturbation on the BUW radiance from that of an altitude change. However, the spectral structures of column and altitude WFs are modulated by the AMF (Figure 2a) and its vertical gradient (Figure 2b), respectively, resulting in broad distinctive wavelength and altitude dependence patterns in the WFs. These broad spectral distinctions between column and altitude WFs at the same altitude and among the same WFs at different altitudes facilitate the retrievals of both absorber column and altitude, because the BUW spectral responses can be attributed to changes in the absorber column and altitude, respectively.

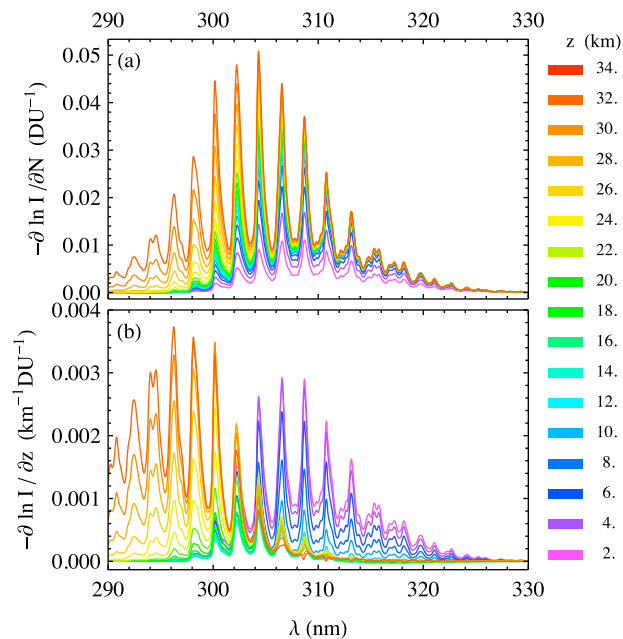


**Figure 3.** (a) Column and (b) altitude weighting functions for a thin SO<sub>2</sub> layer at a set of layer altitudes; conditions as for Figures 1 and 2. When computing these WFs, we have used the measured SO<sub>2</sub> cross sections by *Bogumil et al.* [2003], which have a spectral resolution equal to 0.22 nm below 312.5 and 0.21 nm above 312.5 nm. Note that the instrument specific spectral band pass needs to be applied to these data to obtain the proper WFs for the instrument with a lower spectral resolution.

### 2.3. Sensitivity to SO<sub>2</sub>

[17] Expressions for SO<sub>2</sub> WFs are obtained by multiplying the AMF and its vertical gradient with the temperature-dependent absorption cross sections of SO<sub>2</sub> [*Bogumil et al.*, 2003]. The results are shown in Figure 3, which shows the sensitivity of retrieving atmospheric SO<sub>2</sub> using UV radiance measurements, and how this sensitivity varies with wavelength and SO<sub>2</sub> plume height.

[18] On the basis of WFs in Figure 3, BUW measurements in the range 300–325 nm can be used to detect and quantify SO<sub>2</sub> at all levels of atmosphere. Different subwavelength ranges are sensitive to different SO<sub>2</sub> altitudes: For a high SO<sub>2</sub> plume (>20 km), only measurements below 310 nm have sensitivity to plume altitude; for a plume between 10 and 20 km, BUW measurements in the range 300–310 nm are necessary to estimate the SO<sub>2</sub> altitude; for a plume below 10 km, BUW measurements over the whole range 300–325 nm have the sensitivity to discriminate plume altitude. Measurements in the range 310–325 nm have strong altitude sensitivity for plumes located in the troposphere and this sensitivity reaches its maximum close to the surface.

[19] This analysis of the general absorber column and altitude WFs and their applications to SO<sub>2</sub> is based on the results obtained under the weak-absorption assumption. However, the dependence of these WFs on wavelength and altitude is expected to be similar when the weak absorption assumption is dropped, since the physical mechanisms responsible for carrying the absorber layer altitude and

column information to the TOA UV radiance remain the same regardless of absorber amount. When the amount of absorber is large, the photon contribution from below the absorber layer is reduced more than that above the layer; sensitivity effects can be determined accurately with full radiative transfer calculations using VLIDORT or similar radiative transfer codes with proper input of atmospheric optical properties.

### 3. SO<sub>2</sub> Retrieval

[20] SO<sub>2</sub> released into the atmosphere is usually confined to narrow vertical layers characteristic of localized emissions (such as from volcanoes and power plants), and differential dispersions due to vertical wind shear. Since BUW measurements lack the vertical resolution to resolve details in such layers (c.f. broad peaks in the contribution functions in Figure 1), the most we can expect from the retrieval is an estimation of the layer column and the effective altitude of a SO<sub>2</sub> vertical distribution. This effective altitude is conceptually similar to the optical centroid pressure (or altitude) described by *Joiner et al.* [2010] and *Vasilkov et al.* [2008].

[21] In our forward model, we use the quasi-Gaussian generalized distribution function (GDF) (see Appendix A) with a narrow width (about 1 to 2 km) to represent the vertical SO<sub>2</sub> distribution in a layer. In this case, the effective layer altitude is equal to the central (or “peak”) altitude of the GDF profile. Total column ozone can also be derived from BUW measurements together with these SO<sub>2</sub> layer parameters, and its vertical distribution in the forward model is taken from TOMS V8 climatological ozone profile [*Bhartia and Wellemeyer*, 2002] according to the derived total ozone, the day in the year, and the location (latitude only) of the observation.

[22] Surface reflection and Mie scattering by aerosols and clouds can significantly affect the TOA radiance for wavelengths >300 nm, where photons penetrating the lower troposphere are either backscattered by aerosols/clouds or reflected by the surface. TOA radiance contributions from Mie-scattered photons are highly variable and difficult to model explicitly because of lack of knowledge of their optical properties. Instead, we use the mixed Lambert equivalent reflectivity (MLER) model [*Ahmad et al.*, 2004] to account for the combined effects of surface reflections and Mie scattering from aerosols and clouds. The MLER model treats these Mie scatters as an opaque Lambertian surface above the Earth surface. The cloud fraction arises from the partition of the total TOA radiance into two independent contributions: surface and clouds/aerosols. This cloud fraction depends on the wavelength as the relative contributions to the total by the two components change with wavelength. Hence it is called the effective cloud fraction, in contrast to the geometric cloud fraction, which is independent of wavelength. In practice, one sets the albedo of the cloud surface equal to 0.80 and the albedo of the Earth surface to 0.15 when deriving the cloud fraction from the measurements at a nonozone-absorbing wavelength. The albedo selection for the cloud surface is based on the finding by *Ahmad et al.* [2004], in which they have shown that the MLER model reproduces reasonably well the spectral dependence of TOA UV radiance if the cloud surface is set at 0.8 [*Ahmad et al.*, 2004]. We assume the Earth surface

albedo to be 0.15 in the MLER model. This value is higher than most actual surface reflectivity in the UV, except for snow/ice. Doing so is intended to treat haze, aerosol, and small broken clouds as part of the Earth surface rather than as part of elevated cloud. When the derived effective cloud fraction is equal to either 0 (cloud free) or 1 (fully cloudy), only one Lambertian surface is used. In this case, instead of using the pre-set albedo value, the LER is derived from the spectral measurements. Furthermore, to account for the spectral dependence of the effective cloud fraction or LER, we use a second-order polynomial in wavelength to model the MLER closure parameter. To account for the photon penetration into and backscattered from the cloud, the opaque surface for the cloud is placed at the pressure level equal to the cloud centroid pressure [Joiner *et al.*, 2010, and references therein]. The resulting simplified forward model, which includes only gas absorption and Rayleigh scattering, can simulate the measured radiances and its spectral dependence under a wide range of observing conditions.

### 3.1. EISF Algorithm

[23] The EISF retrieval determines the state vector  $X_p$  of geophysical parameters, which include the total ozone ( $\Omega$ ), the total column of SO<sub>2</sub> ( $\Xi$ ), and the effective SO<sub>2</sub> plume altitude ( $z$ ), and the MLER (second-order) polynomial closure parameters ( $F_c$ ,  $c_1$ ,  $c_2$ ), and a Ring parameter ( $p_{rrs}$ ). The EISF adjusts  $X_p$  iteratively until the cost-function differences between measurements  $I_m$  and forward model calculations  $I_{TOA}$  are minimized for the selected fitting window. Accounting for the total error ( $\varepsilon$ ) that includes both satellite BUUV measurement errors and forward modeling uncertainties, the difference between the measurement and the model computation at a single wavelength at the  $i$ th iteration can be expressed as

$$\ln I_m - \ln I_{TOA} = \sum_{p=1}^3 \Delta X_p \left. \frac{\partial \ln I_{TOA}}{\partial X_p} \right|_{X_p=X_{p_i}} + p_{rrs} \sigma_i^{rrs} + \left( \Delta F_c + \sum_{k=1}^2 c_k (\lambda - \lambda_0)^k \right) \left. \frac{\partial \ln I_{TOA}}{\partial F_c} \right|_{F_c=F_{c_i}} + \varepsilon. \quad (10)$$

Here  $\lambda_0$  is the wavelength at which  $F_c$  is determined, and  $p_{rrs} \sigma_i^{rrs}$  is the ‘‘Ring spectrum,’’ an interference effect caused by inelastic Rotational Raman Scattering (RRS) by air molecules which results in the filling-in of both solar (Fraunhofer) features and trace species absorption signatures (the so-called telluric RRS effect). Adapting Liu *et al.*'s [2005] Ring effect correction approach for the EISF algorithm, we use the method developed by Sioris and Evans [2000] to calculate the Ring reference spectrum  $\sigma^{rrs}$ , which is updated at each iteration step; this method takes into account the viewing geometry and the absorber (ozone and SO<sub>2</sub>) amounts, accurately characterizing the spectral structures of RRS filling-in due to ozone and SO<sub>2</sub> absorption.

[24] Most plumes from SO<sub>2</sub> emissions are below 20 km. In these cases, BUUV radiances below 300 nm have almost no sensitivity to these low altitude plumes as shown in Figure 3. In practice we use measurements in the range 300–335 nm to retrieve SO<sub>2</sub> column and altitude. For volcanic degassing and anthropogenic emissions (which release SO<sub>2</sub> mostly in the lower troposphere), one needs only the longer

wavelengths (>310 nm), where BUUV measurements usually have higher signal to noise ratios.

### 3.2. Aerosol Impacts

[25] SO<sub>2</sub> in the atmosphere is frequently accompanied by aerosols, such as ash in a fresh volcanic plume or sulfate formed by SO<sub>2</sub> conversion. Therefore it is important to investigate the impacts of aerosols on SO<sub>2</sub> retrievals. Aerosol extinction optical thickness and single scattering albedo can be retrieved from BUUV measurements [Krotkov *et al.*, 1997; Torres *et al.*, 1998], but this is difficult in the presence of clouds. In the context of the MLER approach used in this paper, we infer the presence of aerosols using the Aerosol Index (AI) developed for TOMS retrievals [Hsu *et al.*, 1996]. The AI is determined from the spectral contrast of measured TOA reflectance between two UV wavelengths (340 nm and 380 nm in case of Nimbus-7/TOMS, and 331 nm and 360 nm for Earth Probe TOMS and in Version 8 (V8) total column ozone algorithm). However, the V8 AI produced in the operational OMI total ozone product (OMTO3) sometimes fails to detect volcanic ash collocated with SO<sub>2</sub>, because the presence of high SO<sub>2</sub> concentrations causes an error in the TOMS-V8 derived total ozone [Bhartia and Wellemeyer, 2002], which in turn leads to an error in the reflectance calculated at 331 nm, and thence to an erroneous value of the AI.

[26] In equation (10), the first-order coefficient  $c_1$ , i.e., the gradient of the effective cloud fraction or LER in wavelength, quantifies the spectral contrast of the underlying surface, and therefore can serve as a proxy of the presence of aerosols. We introduce a new aerosol index (referred to as  $AI_b$  in the sequel), which is defined as the slope term  $c_1$  multiplied by a constant factor, i.e.,  $AI_b = 2700 * c_1$ . The multiplication factor 2700 is selected to make the  $AI_b$  value similar in magnitude to the TOMS V8 AI (referred to as  $AI_a$  in the sequel) [Bhartia and Wellemeyer, 2002].

[27]  $AI_b$  can be determined directly from the BUUV measurements under almost all observing conditions, including partly cloudy scenes.  $AI_b$  is a measure of the deviation from a pure Rayleigh atmosphere; its sign indicates the presence or absence of absorbing aerosols, and its magnitude relates to both the height and extinction optical thickness: Larger extinction optical thickness and higher altitude of aerosols result in larger observed  $AI_b$ . In many cases,  $AI_b$  behaves very much like the traditional value  $AI_a$ : A positive  $AI_b$  indicates the presence of absorbing aerosols, even with underlying clouds, while a negative  $AI_b$  signifies the absence of absorbing aerosols and the likely presence of non-absorbing aerosols (like sulfate) and/or clouds.

[28] In cases of strong SO<sub>2</sub> absorption, where  $AI_a$  fails, EISF continues to generate reliable values of  $AI_b$ , since the algorithm retrieves the effective surface reflectance more accurately by accounting correctly for both ozone and SO<sub>2</sub> absorption. In contrast, the TOMS V8 ozone algorithm may yield a negative (unphysical) surface reflectance due to the neglect of SO<sub>2</sub> absorption, leading to a breakdown in the computation of  $AI_a$ . Note that  $c_1$  (and thus  $AI_b$ ) is very sensitive to radiometric errors and radiance artifacts, but less so to random errors in the measurements.  $AI_a$  is defined in log-reflectance space at the TOA, whereas  $AI_b$  is defined in the reflectance space at the bottom of the atmosphere (BOA) or at the level of effective cloud-top pressure.

[29] We carry out closed-loop tests with synthetic radiances to quantify SO<sub>2</sub> retrieval errors due to the presence of aerosols. Here, we perform EISF retrievals using a number of synthetic TOA spectra simulated (using VLIDORT) with two types of aerosols (ash and sulfate) [Krotkov *et al.*, 1997; Torres *et al.*, 1998] located below, at the same level as, and above the SO<sub>2</sub> layer. In these tests, the columns of ozone and SO<sub>2</sub> and their vertical distributions are assumed known, so that any differences between the “truth” state vector used to generate synthetic spectra and the EISF-retrieved state vector are due to the impact of aerosols.

[30] First, in the presence of absorbing aerosol (ash), we find (1) a higher SO<sub>2</sub> layer altitude and a lower SO<sub>2</sub> layer column when the aerosol layer with small to moderate extinction optical depth is below the SO<sub>2</sub> layer, and (2) lower SO<sub>2</sub> layer altitude and higher SO<sub>2</sub> layer column for an aerosol layer on the same level or above the SO<sub>2</sub> layer, or when the aerosol layer has a large extinction optical depth. Secondly, a scattering aerosol (sulfate) mostly results in lower SO<sub>2</sub> layer altitude and higher SO<sub>2</sub> layer column; the exception occurs when the sulfate aerosol layer is well below the SO<sub>2</sub> layer, in which case a slight overestimation of SO<sub>2</sub> layer height may happen. In general the differences between truth and retrieved quantities increase with aerosol extinction optical thickness, but decrease with a larger separation between SO<sub>2</sub> and aerosol layers when they are below the SO<sub>2</sub> layer; aerosol (especially nonabsorbing aerosol) layers at the same level as or above the SO<sub>2</sub> layer cause large SO<sub>2</sub> retrieval errors, both in layer column amount and layer altitude. These retrieval behaviors are the algorithmic responses to the combined effects of the complex interactions among molecular and aerosol scattering and absorption, and can be qualitatively explained as follows. An aerosol layer in the atmosphere can effectively raise the altitude of the surface at the lower atmospheric boundary, especially if the aerosol scattering is the dominant effect, such as in the case when a nonabsorbing aerosol or an absorbing aerosol with a large optical thickness is placed in the atmosphere. As a result, a retrieval assuming the atmospheric boundary at the lower surface yields a lower SO<sub>2</sub> altitude and a higher SO<sub>2</sub> column than the true values. For an absorbing aerosol with a small optical thickness located below the SO<sub>2</sub> plume, the effect of an elevated absorbing aerosol layer, which reduces radiance reflected from the surface, results in reduced SO<sub>2</sub> column but enhanced layer height sensitivities compared to those calculated with the EISF forward model that places the aerosol on the surface. Consequently the EISF retrieval underestimates the column and overestimates the layer height.

[31] Aerosol impacts are shown in Figure 4, which contains sample results of closed-loop testing for ash (absorbing and scattering) and sulfate (nonabsorbing) aerosols. The total extinction optical depth  $\tau_{aer} < 1.5$  (at 340 nm). The impact on EISF SO<sub>2</sub> column retrievals is modest (<15%), even for significant aerosol loading (with  $\tau_{aer} \sim 1.0$  at 340 nm, i.e.,  $6 < AI_b < 10$  for ash,  $AI_b \sim -0.7$  for sulfate) when the aerosol is below the SO<sub>2</sub> layer, even though SO<sub>2</sub> altitude error can be large (>25%) under these conditions. In general, errors of EISF-retrieved SO<sub>2</sub> altitude and column due to the presence of aerosols are likely to be less than 15%, because  $AI_b$  is well within the range  $-0.5$  to  $10$  under most observing conditions. These results indicate that the MLER model is

quite effective in accounting for the change in radiance contribution function due to the presence of aerosols. Though the presence of aerosol changes the angular distribution of scattered photons and the apparent reflectivity of the surface, it does not significantly alter the local AMF and its gradient when compared with those of a Rayleigh-only atmosphere with matching reflectivity. As long as the simplified MLER model can make a good approximation to the AMF and its vertical gradient, the EISF retrievals yield reasonable results. The MLER model works less effectively when aerosol layers are above the absorbing trace gas layer, and it breaks down when large aerosol absorptions cause the apparent reflectivity to become negative. When this happens, explicit inclusion of aerosol in the retrieval is needed. In summary, based on the results from closed-loop testing,  $AI_b$  can be used to estimate the errors in the SO<sub>2</sub> retrievals under most observing conditions, without knowing the precise height and optical thickness of the aerosols.

### 3.3. Effects of Inhomogeneity

[32] For point-like emission sources (volcanoes) undergoing advection and dispersion in the atmosphere, horizontal distributions of SO<sub>2</sub> plumes are invariably inhomogeneous, especially near the edges. Furthermore, pixel areas (which increase rapidly with viewing angle for many remote sensing instruments including OMI), range from several hundred to over 1,000 km<sup>2</sup>, are comparable in size to horizontal plume extensions. Typically there are many satellite observations with inhomogeneous SO<sub>2</sub> distributions in the field of view. In general, satellite measurements contain no information on the degree of scene inhomogeneity; forward models invariably assume a homogeneous SO<sub>2</sub> distribution for each observation. Given this assumption, it is important to characterize how this inhomogeneity affects SO<sub>2</sub> retrievals.

[33] To accomplish this, we again resort to closed-loop testing by generating synthetic radiances and performing retrievals using both EISF and ISF algorithms. The synthetic TOA radiances consist of two fractions: The first contains an SO<sub>2</sub> layer specified by column amount and layer altitude, while the second is free of SO<sub>2</sub>. Keeping the total SO<sub>2</sub> column constant, we allow the radiance fraction from the SO<sub>2</sub>-free area to vary from 0 to 1 to simulate the degree of inhomogeneity. We compare the retrieved SO<sub>2</sub> column and layer altitude with the “truth” quantities used in the synthetic spectrum simulation. We perform a second series of tests using the ISF retrieval (no altitude retrieval), again keeping the total SO<sub>2</sub> burden constant while allowing the SO<sub>2</sub>-free fraction to vary; this time we are only looking at the inhomogeneity effect on retrieved column.

[34] Figure 5 shows that ISF retrievals for inhomogeneous scenes always underestimate the total SO<sub>2</sub> column even when the plume height is accurately known, and this underestimation increases as the area fraction of SO<sub>2</sub> within the observation footprint becomes smaller. In contrast, EISF retrievals exhibit more complex behavior, in which the retrieved SO<sub>2</sub> column is not always lower than the true value, and overestimation can occur depending on the inhomogeneity fraction. The EISF-retrieved SO<sub>2</sub> layer altitudes are always lower than those used in the simulation, because a scene with a mixture of SO<sub>2</sub>-free and SO<sub>2</sub>-filled areas has an effective SO<sub>2</sub> altitude lower than the layer

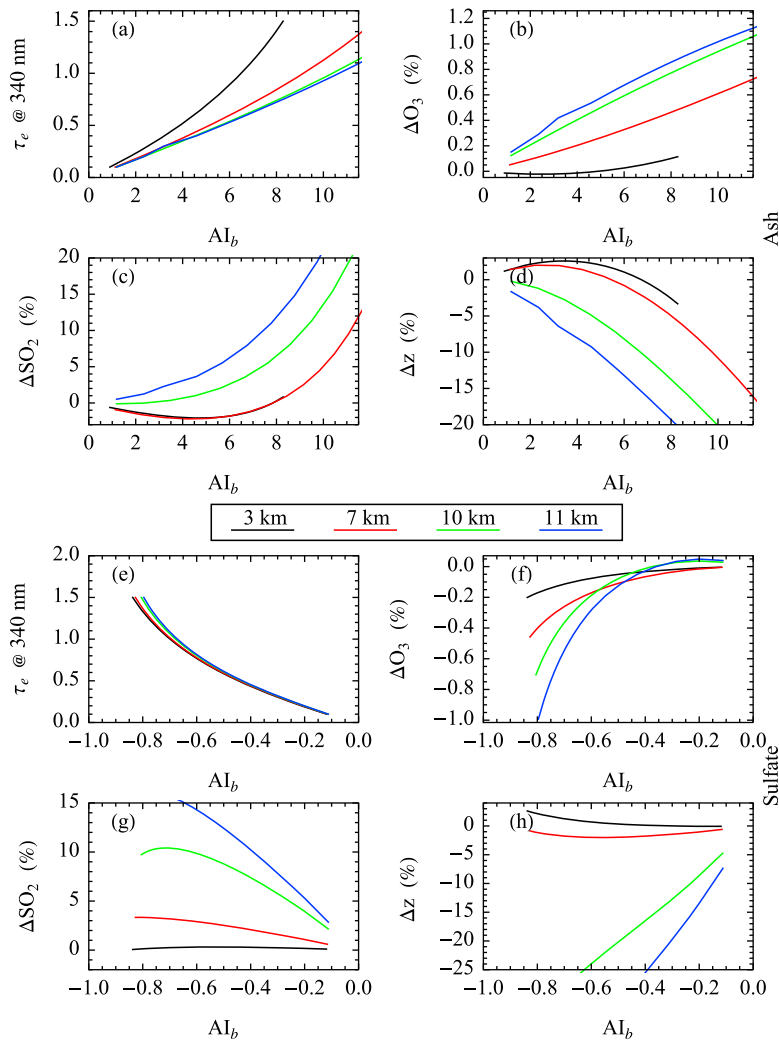


**Figure 4.** Closed-loop EISF retrieval errors for (b and f) ozone, (c and g) SO<sub>2</sub>, and (d and h) SO<sub>2</sub> height, calculated for two types of aerosols (ash and sulfate) [Krotkov *et al.*, 1997; Torres *et al.*, 1998]. The synthetic TOA radiances are calculated for 20° viewing zenith, 50° solar zenith, and 90° relative azimuth angles, with the TOMS-V8 325 DU standard midlatitude ozone profile [Bhartia and Wellemeyer, 2002]. The SO<sub>2</sub> layer is specified by a GDF with peak height at 10 km and a full width at half maximum (FWHM) of 1.8 km. The aerosol layer with extinction optical thickness ( $\tau_{aer}$ ) from 0 to 1.5 is also specified by a GDF with the same FWHM and peak heights at four different locations (3, 7, 10, and 11 km). Figures 4a and 4e show the dependence of  $AI_b$  on both  $\tau_{aer}$  and the height of the aerosol layer.

altitude in the SO<sub>2</sub>-filled area. Clearly the altitude underestimation is larger for smaller fractions of the SO<sub>2</sub>-filled area. Significantly, the EISF-retrieved SO<sub>2</sub> columns are closer to the synthetic “truth” when compared to the ISF results obtained using the true SO<sub>2</sub> layer altitude. In particular, we note that when the SO<sub>2</sub>-filled fraction is large enough (>50%), the error in EISF-retrieved SO<sub>2</sub> column is negligible. Therefore, in order to estimate the total SO<sub>2</sub> burden in a volcanic plume, it is more accurate to derive both SO<sub>2</sub> vertical column and height consistently as in EISF retrievals.

#### 4. Application: 2008 Kasatochi Eruption

[35] With little warning, Kasatochi volcano (52.1775°N, 175.5083°W, 314 m above sea level), a long-dormant

stratovolcano in Alaska’s Aleutian Islands started to erupt explosively on 7 August 2008. A sequence of eruptions was observed between 7 August 2300 UTC and 8 August 0530 UTC by NOAA’s Geostationary Operational Environmental Satellite (GOES). Three distinct eruption plumes were injected into the atmosphere above the local meteorological clouds (<http://cimss.ssec.wisc.edu/goes/blog/archives/709>). These plumes contained large amounts of gases and ash, among which we observed the largest amount (about 2.0 Mt) of sulfur dioxide (SO<sub>2</sub>) released into the atmosphere since the June 1991 eruption of Mount Pinatubo.

[36] OMI, on board the polar-orbiting Sun-synchronous Aura spacecraft launched in July 2004, is a hyperspectral UV and visible instrument, providing daily global contiguous coverage with high spatial resolution (13 × 24 km<sup>2</sup> at nadir). The UV channel is divided into two subchannels,

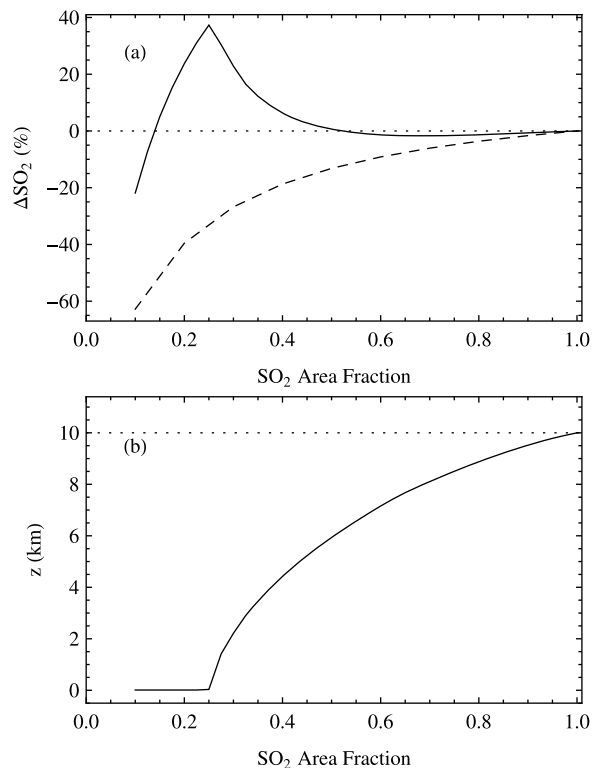


**Figure 5.** Closed-loop EISF and ISF retrieval errors in (a) SO<sub>2</sub> column and (b) SO<sub>2</sub> layer height for degrees of inhomogeneity specified by the fraction of the area that is filled with SO<sub>2</sub>. Synthetic spectra are created for a Rayleigh atmosphere (i.e., no aerosol or cloud) with the TOMS-V8 standard midlatitude ozone profile (with a total column of 325 DU) is used, a 5 DU SO<sub>2</sub> layer described by a GDF with 10 km peak height with a 1.5 km FWHM, and for 15° viewing zenith, 55° solar zenith, and 0° relative azimuth angles. The amount of SO<sub>2</sub> is kept constant, but its area fraction in the field of view varies from 0.1 to 1 in the simulations. Both the EISF and ISF retrievals are done with the assumption that the SO<sub>2</sub> within the field of view is homogeneous. The curves in Figure 5a are SO<sub>2</sub> error for the EISF (solid line) retrievals and for the ISF (dashed line) retrievals assuming the SO<sub>2</sub> layer peak height is fixed (at 10 km). The corresponding EISF retrieved SO<sub>2</sub> layer height is shown in Figure 5b.

UV-2 (310–380 nm) and UV-1 (270–310 nm). The UV-2 channel has a spectral resolution of 0.42 nm and a spectral sampling rate of 0.15 nm/pixel, while the UV-1 channel has a similar spectral resolution and sampling, but with a reduced spatial resolution (13 × 48 km<sup>2</sup> at nadir) due to a much weaker BUV radiance in this wavelength range. Compared to the TOMS instruments, OMI has much higher measurement sensitivity to the presence of aerosols and trace gases. For atmospheric SO<sub>2</sub>, measurement sensitivity has been improved by 2 orders of magnitude compared to that of TOMS [Krotkov *et al.*, 2006]. Using OMI spectra, we can now better quantify SO<sub>2</sub> burdens from anthropogenic emission and volcanic degassing, and measure accurately SO<sub>2</sub> column amounts with simultaneous altitude estimation of the plumes. This progress is in part due to the develop-

ment of new algorithms [Yang *et al.*, 2009a, 2009b] that take full advantage of the hyperspectral measurements.

[37] The OMI operational volcanic SO<sub>2</sub> product is derived from UV-2 measurements using the LF algorithm [Yang *et al.*, 2007], with fast daily SO<sub>2</sub> retrievals over the globe since October 2004. Though the LF does not take full advantage of the hyperspectral data from OMI, it is reasonably accurate in derive small to medium SO<sub>2</sub> columns (<100 DU) and has proved very useful in mapping of all volcanic plumes from degassing to explosive eruptions. For the 2008 Kasatochi eruption, OMI was able to detect and measure (using LF) volcanic SO<sub>2</sub> plumes for over 4 weeks starting on 7 August 2008 when OMI made its first observation of this event. The long-term tracking of the Kasatochi plume and the comparison with trajectory modeling have been analyzed in a separate paper [Krotkov *et al.*, this issue]. Here we focus on the EISF retrievals of Kasatochi plumes for the first few days immediately after the eruption.

[38] The EISF retrievals used both OMI UV-1 and UV-2 measurements covering the spectral range from 300 to 345 nm. We have co-added radiances of two UV-2 pixels in the across-track direction for matching with the corresponding UV-1 measurements, thereby reducing the UV-2 spatial resolution. Note the slope parameter (or equivalently,  $AI_b$ ) for the MLER closure polynomial is mostly determined from measurements >335 nm, where ozone and SO<sub>2</sub> absorption is minimal.

[39] EISF retrievals of Kasatochi plumes are shown in Figure 6, which shows maps of SO<sub>2</sub> columns, effective SO<sub>2</sub> altitudes ( $z$ ), and improved aerosol indices ( $AI_b$ ). Effective plume altitudes for the highest SO<sub>2</sub> pixels are above 10 km, indicating direct injection into the arctic lower stratosphere. Figures 6b, 6e, and 6i show that a small portion of the plume was located above 11 km, and as the plume evolved, this high part seemed to move more slowly than the bulk of the plume (located between 9 and 11 km) that moved southeast and then swirled back northward. The  $AI_b$  maps show that ash fell out of the atmosphere quickly, with  $AI_b$  values decreasing rapidly from the first orbit observations (Figure 6c) to later measurements (Figures 6f and 6j). Note that the effective interior plume altitude shows remarkable consistency despite the drastic change in aerosol loadings, confirming the result from the closed-loop study demonstrating that reasonable retrievals in both height and column amount can be achieved with the MLER model when  $AI_b$  values are not too large. Close to or at the edge of the plume, the retrieved SO<sub>2</sub> effective altitudes are generally quite low. This is consistent with the inhomogeneity effect, which tends to push the retrieved plume altitude toward lower levels. This leads to a more accurate SO<sub>2</sub> column amount from EISF even though the plume altitude is incorrect, as the closed-loop testing has illustrated.

[40] Figure 7 shows the normalized SO<sub>2</sub> column height distribution, calculated as the SO<sub>2</sub> mass at a specific height divided by the total mass of the entire plume, for the three time periods in Figure 6. The peak plume height of the distribution is at 10 km for orbit 21636, while this peak moves to 11.5 km for orbit 21650, and stays at 11 km for orbits 21663 and 21664. This behavior of the retrieved peak value can be qualitatively explained by the two factors (as described in sections 3.3 and 3.4) that affect the EISF height retrievals. Statistically, retrieved plume altitudes are lower

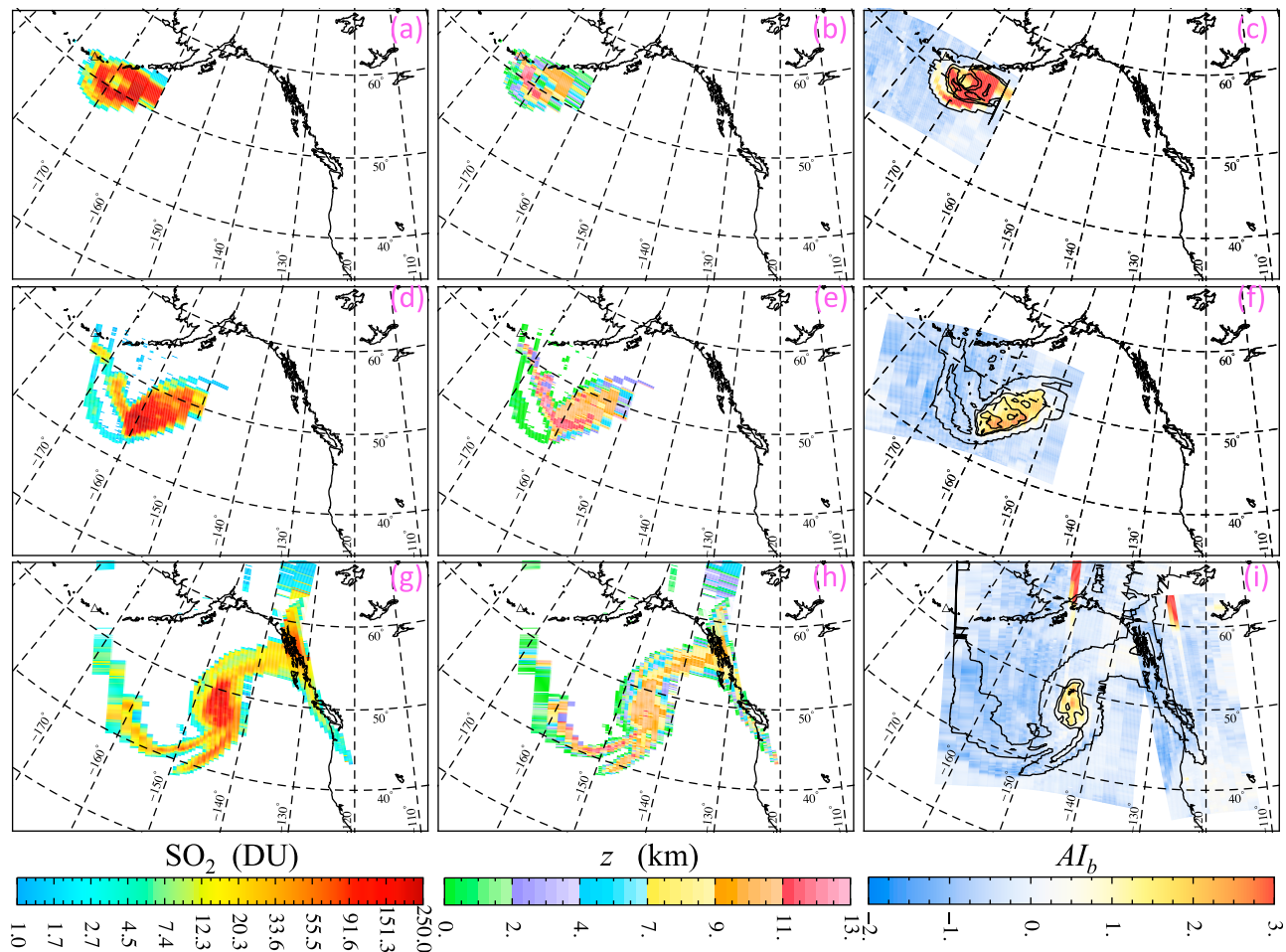


**Figure 6.** EISF retrievals from OMI observations of Kasatochi eruption plumes in three time periods: (a, b, and c) 0056–0103 UT on 9 August 2008, (d, e, and f) 0001–0008 UT on 10 August 2008, and (g, h, and i) 2129–2325 UT on 10 August 2008. Shown are maps of (a, d, g) SO<sub>2</sub> vertical column, (b, e, and h) effective SO<sub>2</sub> layer altitude, and (c, f, and i) aerosol index  $AI_b$ . As indicated in the color scale, only pixels with SO<sub>2</sub> column  $\geq 1$  DU are plotted on the column maps. Correspondingly, only plume heights for pixels shown in the column maps are included in Figures 6b, 6e and 6h. For  $AI_b$ , all the pixels (even those outside the volcanic plumes) are included in Figures 6c, 6f and 6i. The contours shown in the aerosol index maps are equal SO<sub>2</sub> lines from the corresponding SO<sub>2</sub> maps. In Figure 6a for OMI orbit 21636, the maximum SO<sub>2</sub> value is 261 DU at (166.985° W, 49.6296° N), with an effective altitude 10.5 km above sea level (ASL) and  $AI_b = 5.6$ . In Figure 6d for OMI orbit 21650, the maximum SO<sub>2</sub> value is 280 DU at (160.707° W, 45.8713° N) with an effective altitude 10.3 km ASL and  $AI_b = 1.7$ . In Figure 6h for OMI orbits 21663 and 21664, the maximum SO<sub>2</sub> value is 208 DU at (146.425° W, 49.4675° N) with an effective altitude 10.3 km ASL and  $AI_b = 1.7$ . The tonnage for the total SO<sub>2</sub> burden is 1.5 Mt in Figure 6a, 1.6 Mt in Figure 6d, and 2.0 Mt in Figure 6g.

than actual plume altitudes for the initial orbits: This is due to the high ash loadings which are likely located at the same level as the SO<sub>2</sub>, thus causing an underestimation of plume altitude as illustrated by the green curves in Figure 4d. The retrieved altitudes for subsequent observations are not only higher than those from the initial orbit as the ash has fallen out; they are also more accurate. Further plume dispersion increases the inhomogeneity of the SO<sub>2</sub> field; this in turn leads to lower retrieved heights overall, though the interior of the plume should stay at roughly the same height since SO<sub>2</sub> is still quite uniform within the plume.

[41] The total SO<sub>2</sub> burden retrieved for this event peaks at  $\sim 2.0$  Mt on 10 August 2008, from composite observations

of OMI orbits 21663 and 21664. Note that the instrument anomalies (detailed at <http://www.knmi.nl/omi/research/product>) can be clearly identified by the elevated  $AI_b$  above 60°N on Figure 6j) had not yet affected SO<sub>2</sub> retrievals during the first few days immediately after the eruption because the Kasatochi plume was still quite compact and outside the anomaly-affected pixels. Though they are more affected by the instrument anomalies, which tend to increase the retrieved SO<sub>2</sub> columns, the Kasatochi plume tonnage estimates for the subsequent days do not increase (2.0 Mt on 11 August 2008) and start to decrease on 12 August 2008. Therefore we consider this peak SO<sub>2</sub> tonnage (2.0 Mt) to be the total SO<sub>2</sub> emission from Kasatochi during this August

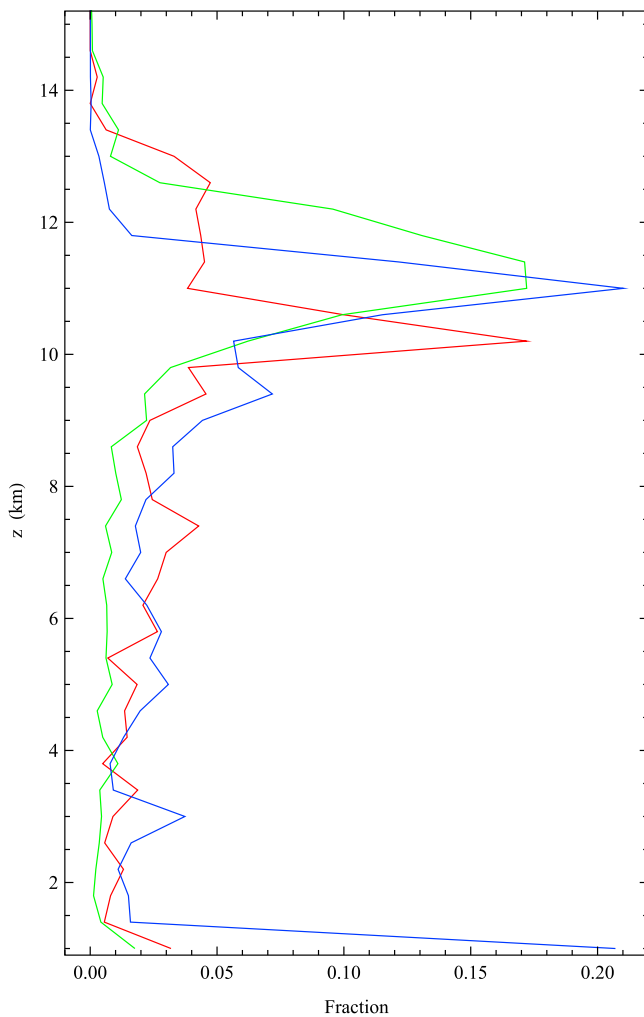


**Figure 7.** Normalized SO<sub>2</sub> column height distribution as a function of layer altitude for the observations shown in Figures 6b (red), 6e (green), and 6i (blue). The bin size for the layer altitude is 0.5 km.

2008 eruption. It is quite likely that a greater SO<sub>2</sub> mass is injected into the atmosphere during this event, as the column retrievals are likely biased low, reducing the estimated total SO<sub>2</sub> tonnage, as is evidenced by the lower tonnages in Figures 6a (1.5 Mt) and 6d (1.6 Mt) relative to Figure 6g. The >20% underestimation of total tonnage from the full plume during the earlier OMI overpasses is very likely due to missed detection of SO<sub>2</sub> partially obscured by the mixtures of thick volcanic ash and clouds. It may also be possible that this tonnage increase is due to subsequent release of SO<sub>2</sub> trapped inside ice crystal or due to the conversion of H<sub>2</sub>S (which may be also released from volcano but are not observed directly) into SO<sub>2</sub>.

## 5. Altitude Comparisons

[42] The altitude of a volcanic plume can be estimated using the backscatter measurement from the CALIOP instrument on board the CALIPSO satellite [Carn *et al.*, 2007] (in NASA's A-Train constellation which also includes Aura). In Figure 8, we compare the OMI-retrieved Kasatochi

SO<sub>2</sub> plume height with the near-coincident CALIOP measurements of vertical profiles of scattering particulates (aerosols or clouds from the eruptions). The OMI effective SO<sub>2</sub> height is close to but slightly beneath the CALIOP plume altitude. Since CALIOP cannot see SO<sub>2</sub> directly and has a much narrower field of view than OMI, we would expect some difference in plume altitude.

[43] Transport modeling is another method frequently used to derive height information from trace gas and aerosol clouds [Schoeberl *et al.*, 1993; Allen *et al.*, 1999] and has recently been used to estimate volcanic SO<sub>2</sub> plume heights [Eckhardt *et al.*, 2008; Hughes, 2009]. There are two predominate approaches used to infer the height of a trace gas or aerosol cloud from trajectory simulations: forward [Schoeberl *et al.*, 1993; Allen *et al.*, 1999; Prata *et al.*, 2007] and backward (or back) [Eckhardt *et al.*, 2008; Hughes, 2009] trajectory modeling.

[44] We use both forward and backward trajectory analyses to infer the height of a specific and highly concentrated region of the Kasatochi SO<sub>2</sub> cloud. A forward trajectory analysis is used to highlight and verify unique transport characteristics partially observed in the direct satellite SO<sub>2</sub> measurements. Back trajectories are then initialized at a highly concentrated region of an SO<sub>2</sub> cloud at the time of satellite observations. The back trajectories said to correctly estimate the SO<sub>2</sub> altitude are found by requiring their dis-

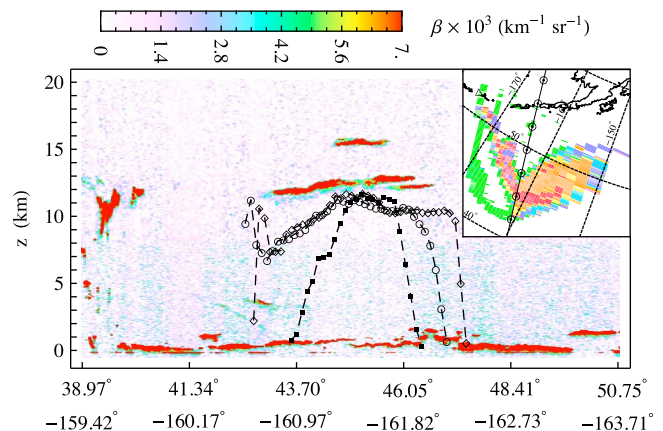


**Figure 8.** The lidar return signals (total attenuated backscatter,  $\beta$ ) from the CALIOP 532 nm channel on 9 August 2008, calibrated in units of  $\text{km}^{-1} \text{sr}^{-1}$ , and the effective SO<sub>2</sub> plume altitudes for three OMI cross-track positions: UV-1 position (1 based indexing scheme), 18 (black square), 19 (empty circle), and 20 (empty diamond). CALIOP version 2.01 data product is used to plot this figure. In the UV-1 channel, the OMI swath Instantaneous Field Of View (IFOV) of  $115^\circ$  (corresponding to 2600 km on the ground) is divided into 30 ground pixels in the swath (across track) direction, with pixels 15 and 16 straddling the nadir viewing direction. Positions 18–20 refer to three slightly off-nadir viewing pixels, on the east side of the satellite orbital track. The inset at the upper right corner is the corresponding OMI plume height map (a subset of Figure 6e), with the CALIPSO ground track shown as the solid black line with the overlaying symbol (circle), lying in between OMI cross-track positions 18 (on the left) and 19 (on the right).

tance of closest approach to the volcano be small [Hughes, 2009] and that they exhibit transport characteristics similar to those seen in the forward trajectory analysis (and satellite observations).

[45] The trajectories used in this study were computed by the University of Maryland, Baltimore County Lagrangian Transport (UMBC-LT) trajectory model, which was adapted from the Goddard Space Flight Center (GSFC) trajectory model [Schoeberl and Sparling, 1995]. The UMBC-LT model is a Lagrangian trajectory model that performs a temporal integration of North American Regional Reanalysis (NARR) [Mesinger et al., 2006] winds to advect passive scalars in the atmosphere, producing trajectories of atmospheric transport. The UMBC-LT model is purely a Lagrangian transport model and does not simulate any chemistry.

[46] The forward trajectories shown in Figure 9a represent the mean path computed from a cluster of 225 trajectories, initialized at six vertically layers above the Kasatochi volcano. These trajectories are plotted over a series of five satellite snapshots of the SO<sub>2</sub> cloud. The pressures denoted for each of these transport paths represent the pressure at which the trajectories were initialized. In general, the pressure along the transport path will change. The most distinctive transport characteristic is the cyclonic motion attributed to entrainment of the SO<sub>2</sub> cloud into a low-pressure system, shown by nearly all the mean forward trajectory paths. The initial cyclonic rotation shown in the mean trajectory paths agrees very well with the first satellite snapshot of the SO<sub>2</sub> cloud. Afterward, the prominence of the rotation motion, over the translational motion, varies depending on the trajectory initialized pressure. The rotational motion is emphasized as two cusps in 200 mbar and 300 mbar initialized mean paths; rotational-to-translational motion on 400 mbar and 500 mbar trajectories is less pronounced, showing only a single cusp. The mean 150 mbar and 600 mbar trajectories tend to diverge from the actual SO<sub>2</sub> transport. It should also be noted that only the 200 mbar and 300 mbar initialized trajectories continue to follow the SO<sub>2</sub> cloud along its full path, the other mean paths eventually deviate from the observed SO<sub>2</sub>.

[47] A backward trajectory analysis was performed from a group of high SO<sub>2</sub> measurements (SO<sub>2</sub> > 100 DU) observed on 11 August 2008 (orbit 21678), Figure 9b. This condition selects a cluster of 78 OMI measurements (a rough outline of this region is shown in figure 9b as a dashed yellow line). Six vertically stacked trajectories were then initialized from each measurement and driven backward in time. Trajectories were grouped based on their initial pressure level and the mean paths were computed. In order to select which

mean trajectory paths were initialized at the correct pressure level, we applied two constraints. First, we require that the trajectories arrive to within a close proximity of the volcano, with respect the other mean trajectory paths. A more detailed analysis of what is considered a close proximity is discussed by Hughes [2009]; however, here it is clear that only the 400 mbar, 300 mbar, and 200 mbar trajectory paths arrive remotely close to the volcano. Next, we apply the second condition that these mean trajectory paths exhibit the correct transport characteristics shown from the forward trajectory analysis. This eliminates the 400 mbar trajectory as a potential transport path. While the 400 mbar trajectories did arrive relatively close to the volcano, the mean path of these trajectories shows little or none of the rotational motion observed in the forward trajectories. The 300 mbar and 200 mbar initialized mean paths both exhibit some potential rotational motion, yet the cusps from the cyclonic motion are more distinct in the 200mbar trajectories. On the basis of the two criteria described above, we infer that the probable height range for the SO<sub>2</sub> plume in the region is between 300 mbar and 200 mbar, or 9.3 km and 11.9 km. This estimate agrees very well with EISF retrieved altitudes, which are between 9 km and 11 km in the same region (see Figure 6i).

## 6. Summary and Conclusions

[48] In this paper, we have elucidated the physical processes responsible for the distinct spectral responses in TOA radiance induced by perturbations in the column and altitude of an absorber. These new insights have resulted in a practical satellite retrieval technique, the EISF algorithm for ozone and SO<sub>2</sub> retrievals from hyperspectral UV measurements. For the first time SO<sub>2</sub> plume altitude can be directly estimated from these measurements. Achieving this also greatly improves the quantification of SO<sub>2</sub> column amounts for a wide variety of conditions. Additionally, the EISF retrieval yields a new and improved UV aerosol index  $AI_b$ , which quantifies the spectral contrast of the atmospherically corrected (by removing the effects of Rayleigh scattering and gaseous absorption) effective surface reflectance (i.e., LER at the bottom of the atmosphere or at the cloud-top pressure level).  $AI_b$  provides a reliable means for absorbing aerosol detection, and it works very well for volcanic ash as demonstrated in this paper.

[49] The performance of the EISF algorithm has been examined using closed-loop testing. We have found that the presence of aerosols (both absorbing and nonabsorbing) do not in general cause large errors (<15%) in EISF retrievals of SO<sub>2</sub> column and its layer altitude under most observing

---

**Figure 9.** Both (a) a forward and (b) a backward trajectory analysis is performed on the 2008 eruption of the Kasatochi volcano, and the mean transport paths are shown. (a) In the forward analysis, six layers of a 15 × 15 grid of trajectories were initialized at six pressure levels above the volcano. These trajectories were started at 0000 UT on 8 August 2008 and computed until 0000 UT on 13 August 2008. The endpoint of the trajectory is denoted with a dot. There are five OMI SO<sub>2</sub> retrievals from 9 to 12 August shown in Figure 9a and four retrievals from 9 to 11 August shown in Figure 9b. (b) In the backward trajectory analysis, six trajectories were initialized at different pressure levels for each measurement of SO<sub>2</sub> > 100 DU on 11 August 2008. The backward trajectories were initialized at the time of the OMI measurement (2300 UT on 11 August) and stopped at 0400 UT on 8 August. The symbols shown along the back trajectory paths represent the overpass times of the orbits: 21636 (squares), 21650 (diamonds), and 21664 (triangles). The location of the volcano is denoted with a star.

conditions:  $-0.5 < Al_b < 10$ , and the aerosols are located below the SO<sub>2</sub> layer. We have also investigated the effects of inhomogeneity, and our findings show that EISF retrievals can yield accurate column amounts even for partially SO<sub>2</sub>-

filled scenes, but always underestimate the plume altitudes for these scenes. When the SO<sub>2</sub>-filled area occupies only a small portion of the field of view, large uncertainties in the retrieved column amounts and severe underestimations of

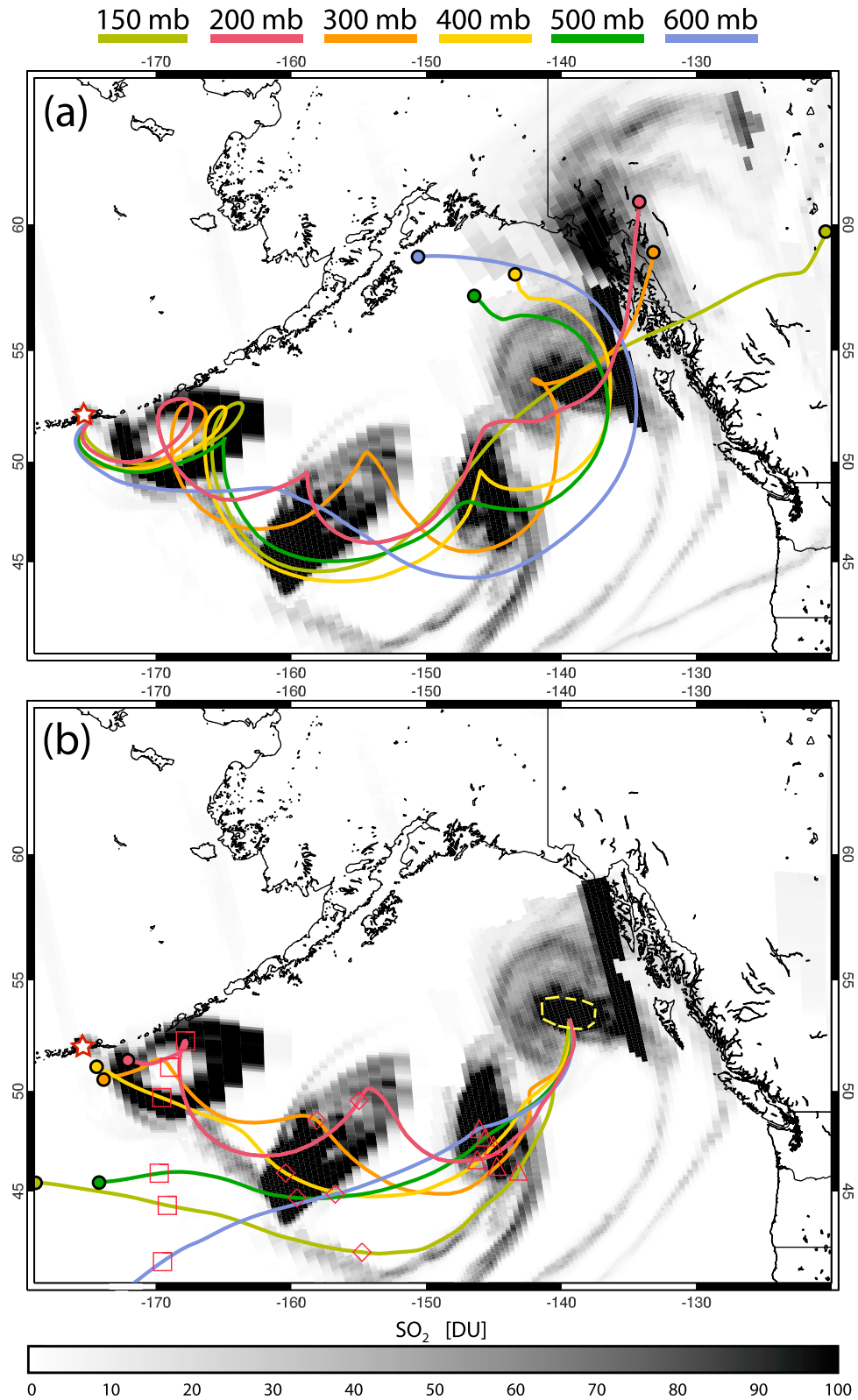


Figure 9

plume altitudes resulted from retrievals based on the homogeneous scene assumption. Therefore instruments with a higher spatial resolution, such as the future TROPOMI (Tropospheric Ozone Monitoring Instrument, with a footprint size of 10 km × 10 km at nadir) [Levelt *et al.*, 2006b], are expected to achieve more accurate measurements of trace gases, especially SO<sub>2</sub>.

[50] The EISF algorithm can be further improved, particularly for inversions under cloud and aerosol conditions, with which large retrieval uncertainties for SO<sub>2</sub> are associated. Since these observing conditions are frequently encountered in satellite observations, reducing the associated uncertainties represents great advances in BUUV retrieval techniques. This can be achieved by extracting cloud and aerosol properties directly from the same hyperspectral UV measurements, which contain more information that is yet to be fully explored.

[51] We have thus far obtained the best assessment of SO<sub>2</sub> burden of the August 2008 Kasatochi eruption from EISF OMI retrievals. The EISF height retrieval was also shown to agree with height information derived from both CALIOP measurements and transport analyses. This eruption was notable for its emissions, releasing at least 2.0 Mt of SO<sub>2</sub>; much of it had reached the upper troposphere and lower stratosphere. This was the largest volcanic SO<sub>2</sub> emission measured by UV satellite remote sensing since 1991, and the largest at high northern latitudes since UV satellite measurements began in 1978.

## Appendix A: GDF

[52] We summarize the generalized distribution function (GDF), used in this paper to parameterize vertically localized distributions of atmospheric constituents (trace gases and aerosols). The GDF profile  $P(z)$  lies between two altitudes  $z_1$  and  $z_2$ , and has its peak value at altitude  $z_0$  between  $z_1$  and  $z_2$ . Mathematically, the GDF has the form

$$P(z) = \frac{N \exp(-h|z - z_0|)}{(1 + \exp(-h|z - z_0|))^2}, \text{ for } z_1 \leq z \leq z_2. \quad (\text{A1})$$

We assume that the profile has a known half width  $w$  and integrates to a total column amount  $\Omega$ . These two conditions will fix the two unknowns  $N$  and  $h$  in (A1). We find

$$\Omega = \int_{z_2}^{z_1} P(z) dz, \text{ (total column)} \quad (\text{A2})$$

$$\frac{\exp(-h|w|)}{(1 + \exp(-h|w|))^2} = \frac{1}{8} \text{ (half width)}. \quad (\text{A3})$$

Solving (A3) yields  $h = \ln(3 + \sqrt{8})/w$ , while solving (A2) yields

$$N = \frac{h\Omega(1 + q_1)(1 + q_2)}{1 + q_1q_2}, \quad (\text{A4})$$

where  $q_1 = \exp(-h|z_1 - z_0|)$  and  $q_2 = \exp(-h|z_2 - z_0|)$ .

[53] To use this parameterization in radiative transfer modeling, we develop the profile as a set of layer columns defined by an input height grid  $\{z_n\}$ ,  $n = 1, N_L$  (the total number of such columns). The layer column  $U_n$  for layer  $n$

is defined as  $U_n = \int_{z_n}^{z_{n-1}} P(z) dz$ . These integrals are easy to evaluate; for example if the layer is wholly above the peak height, we have

$$U_n = \frac{N}{h} \left( \frac{1}{1 + \exp(-h|z_{n-1} - z_0|)} - \frac{1}{1 + \exp(-h|z_n - z_0|)} \right). \quad (\text{A5})$$

To calculate WFs with respect to total column  $\Omega$  and the peak height  $z_0$ , we need the partial derivatives  $\partial U_n / \partial \Omega$  and  $\partial U_n / \partial z_0$  of the layer columns with respect to these quantities; these are obtained by differentiation of (A5).

## Appendix B: Vertical Grid

[54] We describe here the vertical grid used in our radiative transfer (RT) calculations in EISF retrieval. The atmosphere is divided into 101 layers (refers to as RT layers) in equal log pressure: The pressure (in standard atmosphere) at a layer bottom is given by this equation:

$$P_i = 10^{\frac{(i-101)}{20}}, i = 1, 2, 3, \dots, 101, \quad (\text{B1})$$

where  $i$  is the index for the layer, starts at the top of atmosphere (layer 1), and goes to the bottom of the atmosphere (layer 101). The full grid covers 0 to ~81 km, with an average RT layer width is about 0.8 km. The precise layer width depends on the temperature profile of the atmosphere and varies with the layer number. The typical GDF distribution used in our forward model covers a significant number of RT layers, the computed column and altitude WFs are sensitive to continuous changes in the GDF peak height. For example, a GDF with a FWHM = 2.0 km needs six or more RT layer columns to properly represent vertical distribution. Therefore our retrieval precision is not limited by RT layer size, but by the radiance measurement precision.

[55] **Acknowledgments.** This work was supported in part by NASA under grant NNX10AG60G (A Combined EOS Data and GEOS-Chem Modeling Study of the Direct Radiative Forcing of Volcanic Sulfate Aerosols) and by the U.S. OMI Science Team.

## References

- Ahmad, Z., P. K. Bhartia, and N. Krotkov (2004), Spectral properties of BUUV radiation in cloudy atmospheres, *J. Geophys. Res.*, *109*, D01201, doi:10.1029/2003JD003395.
- Allen, D. R., M. R. Schoeberl, and J. R. Herman (1999), Trajectory modeling of aerosol clouds observed by TOMS, *J. Geophys. Res.*, *104*(D22), 27,461–27,471, doi:10.1029/1999JD900763.
- Bhartia, P. K., and C. W. Wellemeyer (2002), OMI TOMS-V8 total O<sub>3</sub> algorithm, in *Algorithm Theoretical Baseline Document: OMI Ozone Products*, edited by P. K. Bhartia, vol. II, ATBD-OMI-02, ver. 2.0. (Available at ftp://jwocky.gsfc.nasa.gov/pub/LLM\_climatology)
- Bhartia, P. K., R. D. McPeters, C. L. Mateer, L. E. Flynn, and C. Wellemeyer (1996), Algorithm for the estimation of vertical ozone profiles from the backscattered ultraviolet technique, *J. Geophys. Res.*, *101*(D13), 18,793–18,806, doi:10.1029/96JD01165.
- Bluth, G. J. S., S. D. Doiron, C. C. Schnetzler, A. J. Krueger, and L. S. Walter (1992), Global tracking of the SO<sub>2</sub> clouds from the June 1991 Mount Pinatubo eruptions, *Geophys. Res. Lett.*, *19*(2), 151–154, doi:10.1029/91GL02792.
- Bogumil, K., et al. (2003), Measurements of molecular absorption spectra with the SCIAMACHY preflight model: Instrument characterization and reference data for atmospheric remote-sensing in the 230–2380 nm region, *J. Photochem. Photobiol. A*, *157*, 167–184, doi:10.1016/S1010-6030(03)00062-5.

- Bréon, F.-M., D. Tanré, and S. Generoso (2002), Aerosol effect on cloud droplet size monitored from satellite, *Science*, *295*, 834–838, doi:10.1126/science.1066434.
- Carn, S. A., A. J. Krueger, N. A. Krotkov, K. Yang, and K. Evans (2008), Tracking volcanic sulfur dioxide clouds for aviation hazard mitigation, *Nat. Hazards*, *51*, 325–343, doi:10.1007/s11069-008-9228-4.
- Carn, S. A., A. J. Krueger, G. J. S. Bluth, S. J. Schaefer, N. A. Krotkov, I. M. Watson, and S. Datta (2003), Volcanic eruption detection by the Total Ozone Mapping Spectrometer (TOMS) instruments: A 22-year record of sulphur dioxide and ash emissions, in *Volcanic Degassing*, edited by C. Oppenheimer, D. M. Pyle, and J. Barclay, *Spec. Publ. Geol. Soc. London*, *213*, 177–202.
- Carn, S. A., N. A. Krotkov, K. Yang, R. M. Hoff, A. J. Prata, A. J. Krueger, S. C. Loughlin, and P. F. Levelt (2007), Extended observations of volcanic SO<sub>2</sub> and sulfate aerosol in the stratosphere, *Atmos. Chem. Phys. Discuss.*, *7*, 2857–2871.
- Clarisse, L., P. F. Coheur, A. J. Prata, D. Hurtmans, A. Razavi, T. Phulpin, J. Hadji-Lazarou, and C. Clerbaux (2008), Tracking and quantifying volcanic SO<sub>2</sub> with IASI, the September 2007 eruption at Jebel at Tair, *Atmos. Chem. Phys.*, *8*, 7723–7734.
- Coldewey-Egbers, M., M. Weber, L. N. Lamsal, R. de Beek, M. Buchwitz, and J. P. Burrows (2005), Total ozone retrieval from GOME UV spectral data using the weighting function DOAS approach, *Atmos. Chem. Phys.*, *5*, 1015–1025, doi:10.5194/acp-5-1015-2005.
- Eckhardt, S., A. J. Prata, P. Seibert, K. Stebel, and A. Stohl (2008), Estimation of the vertical profile of sulfur dioxide injection into the atmosphere by a volcanic eruption using satellite column measurements and inverse transport modeling, *Atmos. Chem. Phys.*, *8*, 3881–3897.
- Eisinger, M., and J. P. Burrows (1998), Tropospheric sulfur dioxide observed by the ERS-2 GOME instrument, *Geophys. Res. Lett.*, *25*(22), 4177–4180, doi:10.1029/1998GL900128.
- Gassó, S. (2008), Satellite observations of the impact of weak volcanic activity on marine clouds, *J. Geophys. Res.*, *113*, D14S19, doi:10.1029/2007JD009106.
- Hsu, N. C., J. R. Herman, P. K. Bhartia, C. J. Seftor, O. Torres, A. M. Thompson, J. F. Gleason, T. F. Eck, and B. N. Holben (1996), Detection of biomass burning smoke from TOMS measurements, *Geophys. Res. Lett.*, *23*(7), 745–748, doi:10.1029/96GL00455.
- Hughes, E. J. (2009), Using horizontal transport characteristics to infer an emission height time series of volcanic SO<sub>2</sub>, 2007–2009, M.S. thesis, Univ. of Md. Baltimore County, Baltimore.
- Joiner, J., A. P. Vasilkov, P. K. Bhartia, G. Wind, S. Platnick, and W. P. Menzel (2010), Detection of multilayer and vertically extended clouds using A-train sensors, *Atmos. Meas. Tech.*, *3*, 233–247.
- Khokhar, M. F., C. Frankenberg, M. Van Roozendaal, S. Beirle, S. Köhl, A. Richter, U. Platt, and T. Wagner (2005), Satellite observations of atmospheric SO<sub>2</sub> from volcanic eruptions during the time-period of 1996–2002, *Adv. Space Res.*, *36*(5), 879–887, doi:10.1016/j.asr.2005.04.114.
- Krotkov, N. A., A. J. Krueger, and P. K. Bhartia (1997), Ultraviolet optical model of volcanic clouds for remote sensing of ash and sulfur dioxide, *J. Geophys. Res.*, *102*(D18), 21,891–21,904, doi:10.1029/97JD01690.
- Krotkov, N. A., S. A. Carn, A. J. Krueger, P. K. Bhartia, and K. Yang (2006), Band residual difference algorithm for retrieval of SO<sub>2</sub> from the Aura Ozone Monitoring Instrument (OMI), *IEEE Trans. Geosci. Remote Sens.*, *44*(5), 1259–1266, doi:10.1109/TGRS.2005.861932.
- Krueger, A. J., L. S. Walter, P. K. Bhartia, C. C. Schnetzler, N. A. Krotkov, I. Sprod, and G. J. S. Bluth (1995), Volcanic sulfur dioxide measurements from the total ozone mapping spectrometer instruments, *J. Geophys. Res.*, *100*(D7), 14,057–14,076, doi:10.1029/95JD01222.
- Lee, C., A. Richter, M. Weber, and J. P. Burrows (2008), SO<sub>2</sub> retrieval from SCIAMACHY using the Weighting Function DOAS (WFDOAS) technique: Comparison with standard DOAS retrieval, *Atmos. Chem. Phys.*, *8*, 6137–6145.
- Lerot, C., M. van Roozendaal, J.-C. Lambert, J. Granville, J. van Gent, D. Loyola, and R. Spurr (2010), The GODFIT algorithm: A direct fitting approach to improve the accuracy of total ozone measurements from GOME, Quadrennial Ozone Symposium 2008 Proceedings, *Int. J. Remote Sens.*, *31*, 543–550, doi:10.1080/01431160902893576.
- Levelt, P. F., G. H. J. van den Oord, M. R. Dobber, A. Mäkki, H. Visser, J. de Vries, P. Stammes, J. Lundell, and H. Saari (2006a), The Ozone Monitoring Instrument, *IEEE Trans. Geosci. Remote Sens.*, *44*(5), 1093–1101, doi:10.1109/TGRS.2006.872333.
- Levelt, P. F., et al. (2006b), TROPOMI and TROP: UV/VIS/NIR/SWIR instruments, *Proc. SPIE*, *6296*, 629–619, doi:10.1117/12.680582.
- Liu, X., K. Chance, C. E. Sioris, R. J. D. Spurr, T. P. Kurosu, R. V. Martin, and M. J. Newchurch (2005), Ozone profile and tropospheric ozone retrievals from the Global Ozone Monitoring Experiment: Algorithm description and validation, *J. Geophys. Res.*, *110*, D20307, doi:10.1029/2005JD006240.
- Mesinger, F., et al. (2006), North American Regional Reanalysis, *Bull. Am. Meteorol. Soc.*, *87*, 343–360.
- Platt, U. (1994), Differential optical absorption spectroscopy (DOAS), in *Air Monitoring by Spectroscopic Techniques*, *Chem. Anal. Ser.*, vol. 127, edited by M. Siegrist, pp. 27–84, John Wiley, New York.
- Prata, A. J., S. A. Carn, A. Stohl, and J. Kerkmann (2007), Long-range transport and fate of a stratospheric volcanic cloud from Soufrière Hills volcano, Montserrat, *Atmos. Chem. Phys.*, *7*, 5093–5103.
- Robock, A. (2000), Volcanic eruption and climate, *Rev. Geophys.*, *38*, 191–219.
- Schoeberl, M. R., and L. Sparling (1995), Trajectory modeling, in *Diagnostic Tools in Atmospheric Physics*, Proc. Int. School of Phys. “Enrico Fermi,” vol. 124, edited by G. Fiocco and G. Visconti, pp. 289–306, IOS Press, Amsterdam.
- Schoeberl, M. R., S. D. Doiron, L. R. Lait, P. A. Newman, and A. J. Krueger (1993), A simulation of the Cerro Hudson SO<sub>2</sub> cloud, *J. Geophys. Res.*, *98*(D2), 2949–2955, doi:10.1029/92JD02517.
- Sioris, C. E., and W. F. J. Evans (2000), Impact of rotational Raman scattering in the O<sub>2</sub> A band, *Geophys. Res. Lett.*, *27*(24), 4085–4088, doi:10.1029/2000GL012231.
- Spurr, R. (2008), LIDORT and VLIDORT: Linearized pseudo-spherical scalar and vector discrete ordinate radiative transfer models for use in remote sensing retrieval problems, in *Light Scattering Reviews*, *3*, edited by A. Kokhanovsky, doi:10.1007/978-3-540-48546-9, Springer, New York.
- Torres, O., P. K. Bhartia, J. R. Herman, Z. Ahmad, and J. Gleason (1998), Derivation of aerosol properties from satellite measurements of backscattered ultraviolet radiation: Theoretical basis, *J. Geophys. Res.*, *103*(D14), 17,099–17,110, doi:10.1029/98JD00900.
- Vasilkov, A., J. Joiner, R. Spurr, P. K. Bhartia, P. Levelt, and G. Stephens (2008), Evaluation of the OMI cloud pressures derived from rotational Raman scattering by comparisons with other satellite data and radiative transfer simulations, *J. Geophys. Res.*, *113*, D15S19, doi:10.1029/2007JD008689.
- Vernier, J. P., et al. (2009), Tropical stratospheric aerosol layer from CALIPSO lidar observations, *J. Geophys. Res.*, *114*, D00H10, doi:10.1029/2009JD011946.
- Winker, D. M., J. Pelon, and M. P. McCormick (2003), The CALIPSO mission: Spaceborne lidar for observation of aerosols and clouds, *Proc. SPIE Int. Soc. Opt. Eng.*, *4893*, 1–11.
- Yang, K., N. A. Krotkov, A. J. Krueger, S. A. Carn, P. K. Bhartia, and P. F. Levelt (2007), Retrieval of large volcanic SO<sub>2</sub> columns from the Aura Ozone Monitoring Instrument: Comparison and limitations, *J. Geophys. Res.*, *112*, D24S43, doi:10.1029/2007JD008825.
- Yang, K., N. A. Krotkov, A. J. Krueger, S. A. Carn, P. K. Bhartia, and P. F. Levelt (2009a), Improving retrieval of volcanic sulfur dioxide from BUV satellite observations, *Geophys. Res. Lett.*, *36*, L03102, doi:10.1029/2008GL036036.
- Yang, K., X. Liu, N. A. Krotkov, A. J. Krueger, and S. A. Carn (2009b), Estimating the altitude of volcanic sulfur dioxide plumes from spaceborne hyperspectral UV measurements, *Geophys. Res. Lett.*, *36*, L10803, doi:10.1029/2009GL038025.

P. K. Bhartia, N. A. Krotkov, X. Liu, and K. Yang, NASA Goddard Space Flight Center, Mail Code 613.3, Greenbelt, MD 20771, USA. (pawan.bhartia@nasa.gov; nickolay.a.krotkov@nasa.gov; xliu@umbc.edu; kai.yang-1@nasa.gov)

S. A. Carn, Michigan Technological University, Houghton, MI 49931, USA. (scarn@mtu.edu)

E. Hughes and A. J. Krueger, Joint Center for Earth Systems Technology, University of Maryland Baltimore County, Baltimore, MD 21228, USA. (eric.hughes@noaa.gov; akrueger@umbc.edu)

R. J. D. Spurr, RT Solutions, Inc., 9 Channing St., Cambridge, MA 02138, USA. (rtsolutions@verizon.net)

S. G. Trahan, Department of Physics, University of Maryland Baltimore County, Baltimore, MD 21228, USA.